

Chapter 2

General review of molecular MQDT

For over a century, spectroscopy has served as a faithful midwife for the birth of countless new discoveries in modern chemistry and physics. Bohr's theory of the atom was designed to accommodate classical stoichiometric concepts of valency to explain the spectra of hydrogen and alkali atoms. Organic chemists depend on infrared spectroscopy to detect the presence of certain bond types, and the study photoelectron spectra in the visible and ultraviolet regions to draw inferences about the distribution of electrons within those bonds. Biologists utilize the sensitivity of fluorescence decay lifetimes to perturbation by analyte atoms and molecules in order to perform image mapping of cellular structure. The reflectance and emission spectra of rocks and minerals provide clues to geological history, whether of the upheaval of the Earth's crust or of the flow of ancient rivers on Mars. Astronomers rely on spectroscopic observations to determine the composition of stars, as well as their distance, their age, their motion, their temperature, the influence of any extra-solar planets they might support, and the density and composition of the diffuse interstellar matter through which their light subsequently travels. The most accurate clocks in the world depend on spectroscopic standards, as does the definition of the SI unit of length, the meter. The spectroscopic study of distant galaxies and quasars is essential to the pursuit of fundamental cosmological questions regarding the distribution of matter in the universe, its age and early history, and the possible variation of fundamental physical constants over cosmic time scales.

The richness of the information available from spectroscopic analysis is belied by its complexity. The farther removed one becomes from the simple picture of transitions between discrete hydrogenic levels, the more difficult it becomes to make sense of the dense forest of spectroscopic features that encode the details of an atom or molecule's nanoscale structure and dynamics.¹ This onset of complexity may be related to several successive complications of the primitive hydrogenic picture: first, the transition to systems with multiple interacting electrons; second, the passage beyond bound state transitions to the consideration of excitations into the scattering continuum; third, the existence of multiple internal degrees of freedom that may be simultaneously excited, and subsequently exchange energy with one another.

This thesis will be concerned with the resonant continuum spectroscopy of atoms and molecules, for which all three complications are potentially present and important. By the “continuum”, we refer to any region of the spectrum that describes complete separation of two fragment particles, either of an electron from its parent atom, molecule, or ion, or of two dissociative fragments that result from the cleavage of a bond in a molecule or molecular ion. Since the potential energy of separating fragments is not subject to quantization, the states of the continuum region are continuously distributed. The spectrum of such a region, however, will in general display quite complex and irregular peak and valley structures that signify the presence of resonant scattering effects. The distribution, shape, width, and intensity of these features reflect the geometric configuration and dynamic evolution of the system during the brief period in which fragmentation occurs.²

Throughout this chapter, as well as in chapter 5, molecular hydrogen is used for illustrative purposes, as well as for various example calculations. Molecular hydrogen

¹ The British biologist and Nobel Laureate Francis Crick famously described the interpretation of a complicated biomolecular spectra as being “like trying to determine the structure of a piano by listening to the sound it made while being dropped down a flight of stairs.”

² The material in this introduction, and the two sections following, is discussed in most introductory graduate level atomic/molecular physics textbooks. See, for example, chapters 9-12 of [25] or chapters 1-3 of [26].

is a homonuclear diatomic, and as such it is characterized by greater symmetry than heteronuclear diatomic or polyatomic molecules. This greatly simplifies the analytical form of many expressions, sacrificing generality for the sake of improved conceptual clarity. For sake of comparison, some discussion and computational results for the more complicated diatomics N_2 and NO can be found in [27], and a recent example of the successful application of quantum defect theory to a simple polyatomic system is presented in [28].

2.1 Degrees of freedom in molecular physics

In a molecular system, there are four classes of motion: electronic, vibrational, rotational, and translational. Since all inertial frames of reference are physically equivalent, the translational motion can be eliminated by a transformation to the rest frame of the molecule, with no effect on the observed spectrum other than an overall Doppler shift. (For a macroscopic sample, of course, translational motion is randomized and these effects are averaged over many atoms, imposing a limit on experimental resolution.) All other motions, however, are fully quantized, potentially spectroscopically active (subject to the relevant symmetry-dependent selection rules), and in general define degrees of freedom in which energy can be stored and potentially transferred by coupling to the other degrees of freedom.

The fact that the motion can be resolved in this way is a consequence of the differing energy scales with respect to which these motions occur. The separation between electronic energy levels is commonly on the order of a few tenths of an atomic unit, at least for the lowest levels, and the associated transitions appear as lines in the visible or ultraviolet. The separation between vibrational levels is on the order of thousandths of atomic units (10^2 to 10^4 cm^{-1}), and appears in the infrared. The separation between rotational levels is on the order of hundreds of thousandths of an atomic unit (10^0 to 10^2 cm^{-1}), extending into the far infrared or microwave. These figures are all approx-

imate, of course, and the vibrational and rotational level splittings depend specifically on the masses of the nuclei; molecular hydrogen and its isotopomers have light nuclei (protons or deuterons), for example, and thus their splittings are increased by an order of magnitude relative to a heavier molecule like NO.

Table 2.1 shows the level spacings for molecular hydrogen relative to the ground state. This data is representative of the literature references used to check the accuracy of the rovibronic energy levels in my own computations. For extended discussion of the techniques used to calculate these and similar quantities, including the absolute dissociation threshold energy of the H_2^+ and HD^+ molecular ions that are used to fix the spectrum relative to threshold in the example calculations, see [29, 30, 31, 32, 33, 34].

Table 2.1: Tabulation of the lowest rovibrational levels for molecular hydrogen, in cm^{-1} , based on the *ab initio* data of [35]. These values reflect the inclusion of both adiabatic and nonadiabatic correction terms beyond the Born-Oppenheimer approximation.

v	J=0	J=1	J=2
0	0.0	118.5	354.4
1	4161.2	4273.8	4497.9
2	8087.0	8193.8	8406.4
3	11782.5	11883.6	12084.8
4	15250.5	15345.9	15535.8
5	18492.1	18581.9	18760.5

The time scale associated with motion in a particular degree of freedom is inversely proportional to its energy splittings, and thus the differences in energy scale can also be interpreted as defining a hierarchy of time scales. Rotational motion is much slower than vibrational motion, and both are slow relative to electronic motion. Conceptually this means that an electron experiences the nuclear structure of a molecule as “fixed in space”; the nuclei, inversely, experience the electron only as a highly averaged spatial distribution of its motion. The result is an approximate separability of the equations of motion governing these two disparate degrees of freedom; when this assumption is taken to be exact, the result is the familiar *Born-Oppenheimer approximation*. To find

a Born-Oppenheimer solution, the nuclei are first frozen in space, and the electronic Hamiltonian diagonalized subject to the potential for that configuration. The electronic calculation is repeated for a systematically varied range of nuclear coordinate values, mapping out variation in energy levels to define associated potential surfaces. The potential surface is then used to define a Hamiltonian controlling the nuclear motion, which is diagonalized for the vibrational energy spectrum and vibrational wavefunctions.

Figure 2.1 shows the lowest electronic singlet *ungerade* potential curves for molecular hydrogen and the Rydberg series limiting curve of the molecular ion, based on data from the *ab initio* calculations of Kolos and Wolniewicz. Notice the avoided crossing in the $4^1\Sigma_u$ curve, resulting from the crossing of a repulsive electronically autoionizing (doubly excited) state potential curve that descends through this region, creating a similar series of avoided crossings with all of the singly excited electronic states higher than $n=4$.

At the level of the adiabatic approximation, the quantum defect may be defined in the molecular body frame as a function of the internuclear separation R ,

$$U_{n\Lambda}(R) = U_{1s\sigma}^+(R) - \frac{1}{2}[n - \mu_\Lambda(R)]^{-2}. \quad (2.1)$$

In practice, the quantum defect function $\mu_\Lambda(R)$ has a weak energy dependence, although it rapidly approaches an energy-independent value for increasing principal quantum number n . For energy-independent quantum defect calculations, the quantum defect must be defined either relative to one particular potential curve, or else through some limiting procedure in the energy. As an additional approximation, the curves are here diabatically continued through the avoided crossings, since the relation in Eq. 2.1 assumes there are no avoided crossings with other electronic states. (This is a reasonable approximation for the *ungerade* states reached in ground state photoionization of H_2 , since the avoided crossings appear outside the Franck-Condon region and have little

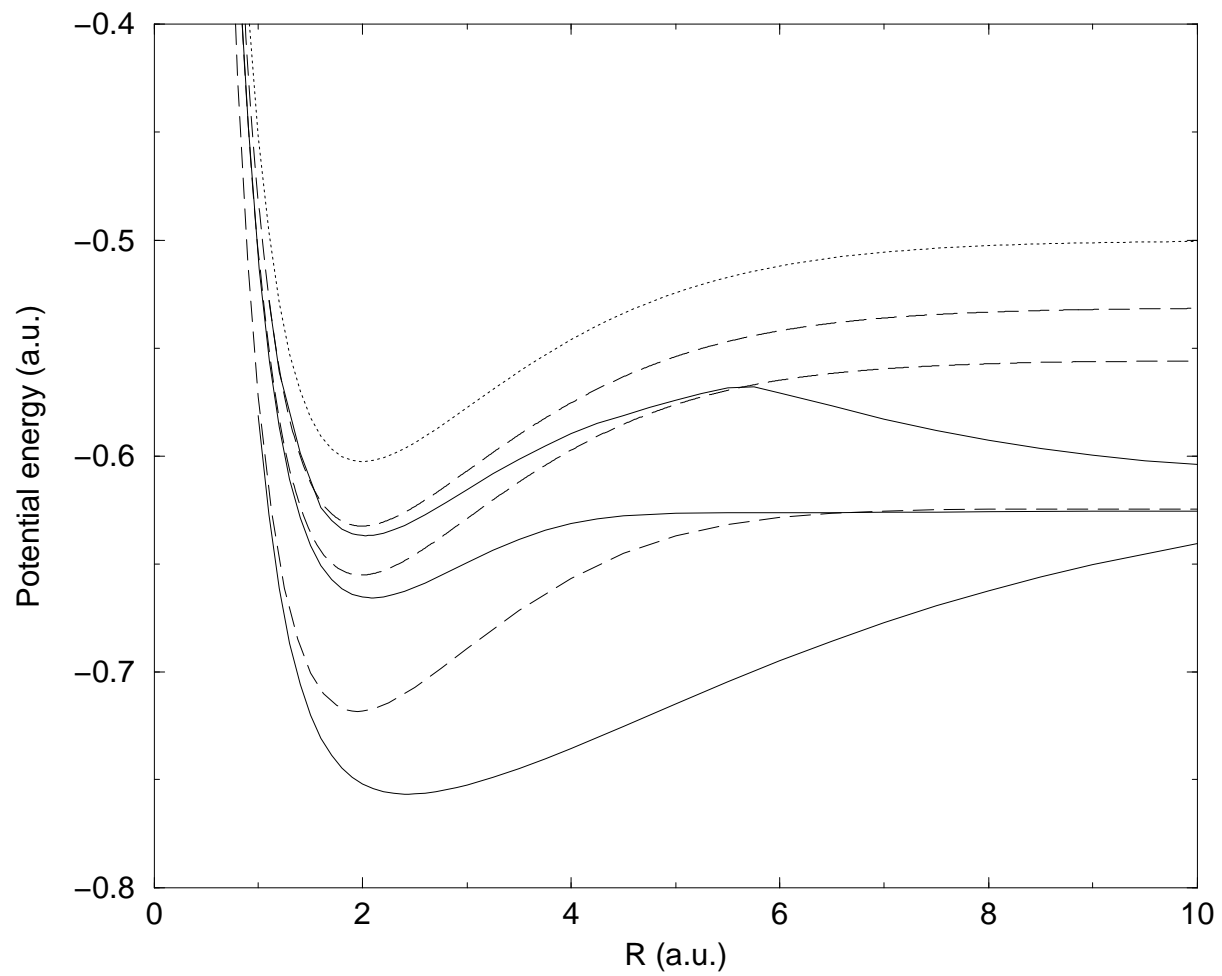


Figure 2.1: Potential energy curves for the Σ (solid) and Π (dashed) symmetries of H_2 , together with the ionic potential curve (dotted), based on the *ab initio* calculations of Kolos and Wolniewicz [36].

influence on the preionization spectrum.) For the sake of all remaining calculations in this section, we will use the 5Σ and 6Π potential curves to define the energy-independent quantum defects, as shown in Figure 2.2. The potential curves associated with these defects are shown in Figure 2.3, giving some visual estimation of the extent of the approximation involved in neglecting energy dependence. The most obvious error is the catastrophic failure of the 2Σ state to reach the correct asymptotic limit. The higher Rydberg states that dominate the continuum spectrum, however, are quite well described by the energy independent approximation. Corrections to this approximation are discussed in [37, 38, 39].

The rotation and vibration of a molecule are coupled more strongly than the nuclear and electronic degrees of freedom, by a combination of centrifugal and Coriolis-like terms of the Hamiltonian. In general, one should not speak of separable vibrational and rotational states, but only a fully coupled “rovibrational” state that obeys the entire nuclear Hamiltonian. To a good approximation, however, the energy of such a state is still recognizable as the combination of a rotational excitation and a vibrational excitation, provided the rotational excitation is small.

The coupling between rotation and electronic angular momentum is particularly sensitive to the excitation of the Rydberg electron. The low temperature spectrum of molecular hydrogen is strongly influenced by an l -uncoupling process, whereby the electron undergoes a gradual transition from the low n case of being strongly coupled to the internuclear axis (Hund’s case [b], where the approximately “good” quantum number Λ is the projection of the total orbital angular momentum onto the internuclear axis) to the high n case where the electronic angular momentum decouples from the symmetry axis and is instead quantized along the ionic core’s axis of rotation (Hund’s case [d], where the approximately “good” quantum number N^+ is the rotational angular momentum of the core). In the range $n=6-10$, the coupling is mixed, and both Λ and N^+ are only meaningful in an approximate sense.

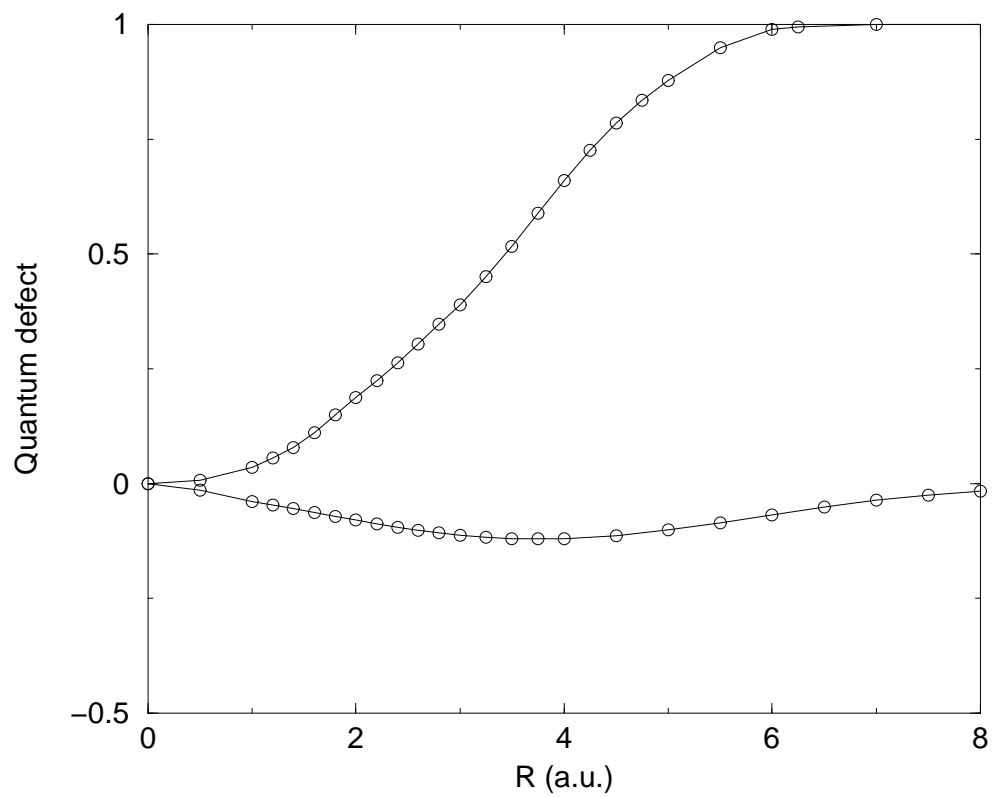


Figure 2.2: Quantum defects for the Σ (solid) and Π (dashed) symmetries of H_2 , based on the fittings of Jungen and Atabek [40].

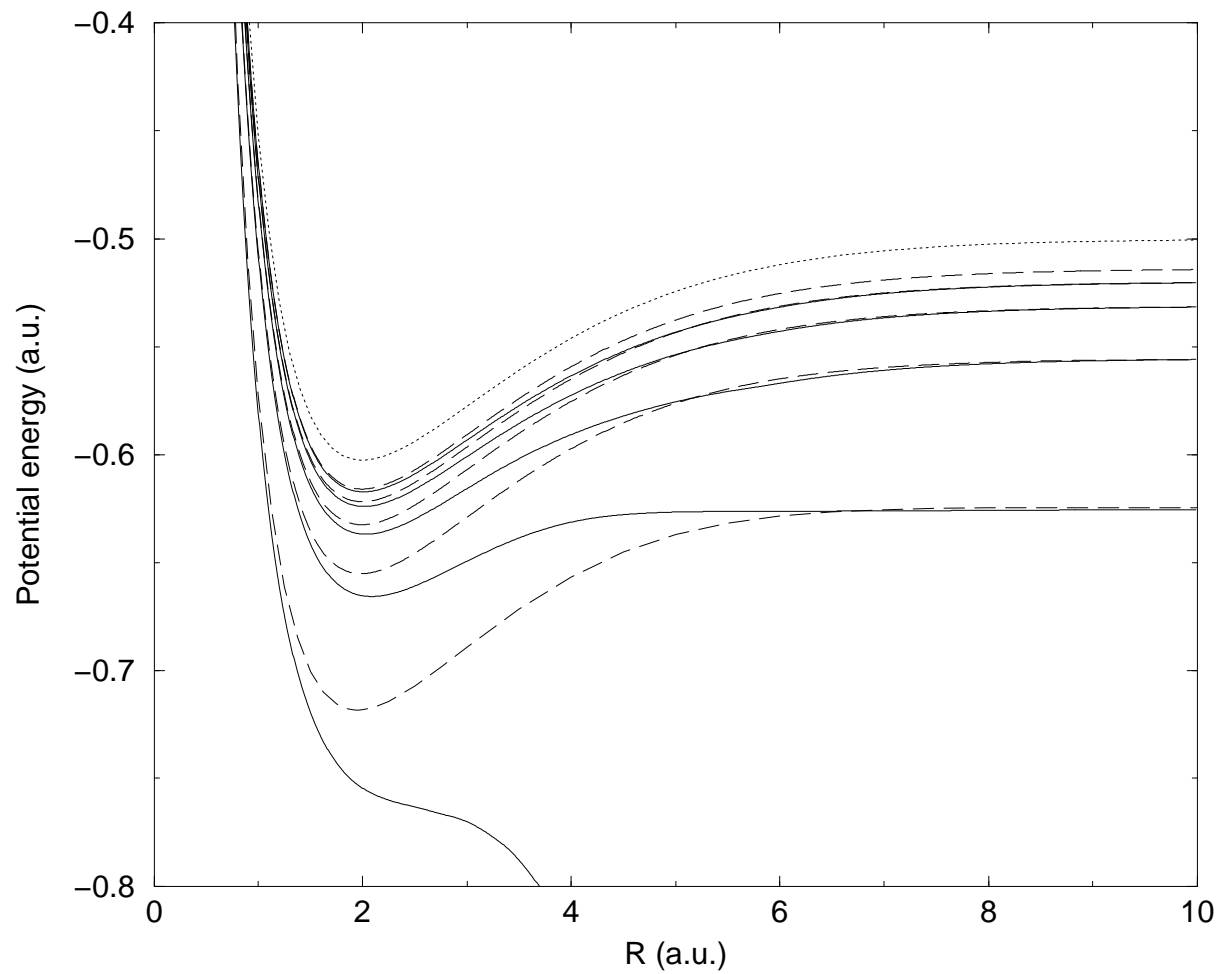


Figure 2.3: Effective energy-independent potential energy curves for the Σ (solid) and Π (dashed) symmetries of H_2 , based on the quantum defects in Figure 2.2, together with the ionic potential curve.

2.2 Resonances

In phenomenological terms, a resonance in the continuum scattering behavior of a dynamical system appears as a strong and localized energy dependence. This may manifest itself as either an enhancement or a suppression of the background cross-section. Mathematically speaking, a resonance is associated with the existence of a nearly bound state of the Hamiltonian, an approximate eigensolution that would become a true bound state if the Hamiltonian were modified in some intentional way. Resonances in atomic and molecular physics result in continuum wavefunctions that accumulate probability density in some restricted region of configuration space for which the magnitude of the separation between the scattering particles is “small”, such that it resembles the distribution of a bound state wavefunction of the two-particle system. If a state at a resonant energy is initially prepared in a superposition that gives it a spatial distribution localized in this way, it will generally remain localized for a long period of time before slowly decaying into the exterior continuum region; in time dependent terms, a resonance can be described as a decaying nearly-bound state, with an associated lifetime inversely proportional to the strength of its coupling to the surrounding continuum.

Resonances commonly arise from one of two situations. A *shape* resonance occurs when the single-channel potential describing the interaction of two particles has a local maximum separating two regions, and the scattering energy is below the energy of this maximum such that it lies at what would become a bound state in the inner region if the potential beyond the local maximum were replaced by an infinite wall. In the time-dependent picture, a particle must travel back and forth between these regions by tunneling through the potential barrier; since tunneling probability is exponentially sensitive to the height of the barrier, the particle can be effectively trapped inside the inner region for a duration sufficient to complete many cycles of the orbital period appropriate for classical motion within the local potential well. Shape resonances in

electron-atom or atom-atom interactions are commonly encountered as a result of the centrifugal correction to the effective potential arising from the $\frac{(l+1)l}{2r^2}$ repulsive term; attractive interactions are typically shorter-range, and thus the cross-over between the strong but shorter-range attractive potential region and the weaker but longer-range repulsive potential region creates a local maximum close to threshold for scattering states with a finite angular momentum.

A *Feshbach* resonance is the result of coupling between channels associated with the excitation of additional degrees of freedom in a system. For example, the energy associated with two electrons being simultaneously excited to hydrogenic Rydberg states would, in the absence of electron correlation, be a stable doubly excited state. Since one of the two electrons may relax back into the ground state and give up its energy to promote the other into the continuum, the doubly excited state is unstable with respect to autoionization, and the two-particle bound state solution instead becomes a resonance. In molecular systems, autoionizing resonances can also result from coupling to the nuclear degrees of freedom. Because of small terms in the Hamiltonian that violate the Born-Oppenheimer assumptions and introduce coupling between the nuclear and electronic motion, a system excited in both a nuclear and an electron degree of freedom is unstable with respect to transfer of energy from the nuclear excitation into the electron (if it has a total energy greater than the ionization threshold). As a result, the electron is able to escape into the continuum. At the energy of the hypothetically uncoupled doubly-excited state, the continuum will show a *preionization* resonance, a resonance that reflects the existence of a short-lived metastable state that eventually undergoes ionization. Similarly, if the hypothetical doubly-excited system is above the energy required for dissociation, the electron can relax to a lower energy level, transferring its energy to the nuclear motion and yielding a *predissociation* resonance. If both types of continua are energetically accessible at once, then the processes will compete, with relative intensities of the preionization and predissociation spectra at that energy that

correspond to the probabilistic branching ratio between the two processes. (we shall set aside the question of predissociation until Chapter 5, and for the moment limit attention to the preionization spectrum.)

Bound states are characterized by a single intensity parameter, governed (in the limit of the dipole approximation) by the dipole oscillator strength of that transition. The width of a bound state transition line is generally controlled by spectral broadening effects that arise from the finite thermal energy of the sample; as the temperature is decreased, the lines become sharper. Bound state transition lines cannot be made arbitrarily narrow, however, due to the natural linewidth arising from their finite lifetime for decay back to the ground state. Resonances, on the other hand, have a natural width associated with the much faster time scale for energy interchange between coupled degrees of freedom; they can correspondingly display much larger linewidths. The shape of a bound state transition line is usually a symmetric Gaussian, in accordance with the exponential Maxwell distribution of kinetic energies at finite temperature. Resonances, by contrast, have a (potentially asymmetrical) Fano line shape. The asymmetry can be explained by recognizing that the excitation to the continuum can occur either by a direct pathway (just as at non-resonant energies), or by the creation of the intermediate autoionizing state; these two pathways must be summed coherently, and thus could give rise to either destructive interference (suppressing the intensity) or constructive interference (enhancing the intensity). Depending on the value of the lineshape parameter, the peak may even be converted into a window resonance, a nearly symmetric dip in the cross-section.

In the limit of extremely weak coupling (and thus extremely long decay lifetime), resonances strongly resemble bound states. Indeed, as the coupling vanishes, a resonance must pass over smoothly into a true bound state embedded in the continuum. Although the continuum itself is uniformly and densely packed with states, it is possible to imagine taking a carefully arranged linear combination of continuum wavefunctions

(with, in general, complex coefficients) that behaves very much like a discrete eigenstate [41, 42]. In particular, it will display time dependence proportional to $e^{iE_a t}$, where E_a is a complex value; the real part of E_a describes periodic motion within the local quasi-binding potential, and the imaginary part describes the slow leak of electron probability density into the rest of the continuum. This complex energy state is in some sense the optimally discretized eigenstate of the Hamiltonian for representing that particular resonant process; it is a true pole of the scattering Green's function, analytically continued into the complex plane. One can imagine performing the same transformation in the other direction; taking a finite basis of such scattering eigenstates, and using them as a representation of a portion of the continuum. we shall revisit this idea in chapter 5.

For the Coulomb potential of an electron in a neutral molecule, there exists an infinite number of excited electronic Rydberg states. The ionizing electron leaves behind a molecular ion which may be in either the ground state or any energetically accessible rotationally or vibrationally excited state. The residual state, in conjunction with all other quantum numbers needed to describe the escaping electron, is termed a *channel*, and labeled by the appropriate rotational or vibrational quantum numbers of the molecular ion. (The use of asymptotic states to define the channel labels provides a natural connection with the scattering matrix (or S-matrix) representation of the scattered continuum wavefunction—the indices of the S-matrix correspond to the asymptotic channels.) The energy at which a channel becomes energetically accessible, or *open*, is simply the energy of the molecular ion in that rotational and vibrational state. At lower energies, the channel is closed, but still influences the continuum by creating an infinite series of Rydberg resonances. Unlike bound state transitions, which have experimental widths that reflect an incoherent sum over many particles in a sample, resonances can (and frequently do) overlap with one another and produce complicated interference effects. In particular, resonances belonging to a Rydberg series attached to one channel threshold may interact with resonances belonging to a different channel threshold. If the

two series have distinct properties— say, one has broad widths and decays primarily by ionization, and the other is narrow and decays primarily by dissociation— the composite effect on the (coherent) total spectra can be quite complex and difficult to untangle. Surmounting this difficulty is the principal task of theoretical multichannel Rydberg spectroscopy, known more commonly in the literature as multichannel quantum defect theory (MQDT).

2.3 Channel elimination: Traditional and energy-smoothed approaches

Quantum defect theory begins from the assumption that the N_o independent solutions of an N_o -channel Schrödinger equation can be written as an expansion with terms consisting of a product of channel functions (describing the state of the core and all degrees of freedom of the outer electron except the fragmentation coordinate) and a linear combination of radial Coulomb functions. These long range solutions, valid beyond the region where channel coupling remains significant, can be written in more than one representation, but a convenient choice for conceptual purposes is the outgoing wave form

$$\Psi_i^{phys}(E) = \mathbf{A} \sum_i^{N_o} \frac{1}{r} \Phi_i(\omega) [f_i^+(r) S_{ii'}^{phys} - f_i^-(r) \delta_{ii'}], \quad r \rightarrow \infty, \quad (2.2)$$

where the scattering matrix is labeled with the superscript *phys* to denote that only channels which are energetically accessible (open) will contribute to the sum. The Coulomb functions $f_i^\pm(r)$ are those that obey incoming and outgoing wave boundary conditions [43], and the operator \mathbf{A} denotes a formal antisymmetrization procedure. In this expression, $\Phi_i(\omega)$ includes the total wavefunction of the core associated with ionic threshold energy E_i , and the spherical harmonics $Y_{lm}(\theta, \phi)$ and spin wavefunction of the outer electron. For the example system of molecular hydrogen, we adopt the approximation that only *p*-wave scattering contributes to the state probed in total

absorption— even parity states are symmetry forbidden transitions, and f and higher partial waves are unable to penetrate through the centrifugal barrier into the coupling region— and thus the index i describes only the vibrational and rotational states v^+, N^+ of the core. (In fact, for the calculation for HD in the following section the breakdown of *gerade-ungerade* symmetry compromises the accuracy of this approximation, but this is expected to only be significant in the vicinity of the dissociative thresholds of highly excited vibrational states.)

The critical point realized by Seaton, Fano, and other MQDT pioneers is that the asymptotic boundary conditions implied by the above expression need not be enforced until the final stage of the calculation. The short range interactions involved in the creation of auto-ionizing resonances can be fully included by the use of an alternate expansion that incorporates an additional N_c accessible excitation channels, whose Rydberg electron channel energies are below the threshold for ionization. This modified expression is still only accurate beyond some value r_0 bounding the small- r region where coupling occurs, and can be written in the similar form

$$\Psi_{i'}(E) = \mathbf{A} \sum_i^N \frac{1}{r} \Phi_i(\omega) \frac{1}{i\sqrt{2}} [f_i^+(r) S_{ii'} - f_i^-(r) \delta_{ii'}], r > r_0. \quad (2.3)$$

Here $S_{ii'}$ indicates a quantity familiar in multichannel quantum defect studies, the *smooth, short-range* N-channel scattering matrix.

Roughly speaking, the i' -th independent solution in Eq. (2.3) describes a simple one-step scattering process in which the outermost electron encounters the ionic core while moving inward in channel i' , and scatters outward into all channels i . Some of the i channels may be energetically closed at $r \rightarrow \infty$, but the finiteness boundary condition has not yet been imposed.

In order to remove unphysical closed-channel divergences, the usual MQDT “channel-elimination” procedure is employed, which amounts to forming an appropriate linear

combination of the solutions in Eq. (2.3) to construct the physical scattering matrix. We write this expression in the form used in Ref. [44], in terms of the Hermitian conjugate of S , partitioned into open and closed sub-blocks:

$$\mathbf{S}^{\dagger phys} = \mathbf{S}_{oo}^{\dagger} - \mathbf{S}_{oc}^{\dagger} [\mathbf{S}_{cc}^{\dagger} - e^{2i\beta}]^{-1} \mathbf{S}_{co}^{\dagger}. \quad (2.4)$$

The four matrices in the right-hand side of (2.4) are physically open and closed partitions of the smooth, short-range scattering matrix (Hermitian conjugated) from Eq. (2.3),

$$\mathbf{S}^{\dagger} = \begin{pmatrix} \mathbf{S}_{oo}^{\dagger} & \mathbf{S}_{oc}^{\dagger} \\ \mathbf{S}_{co}^{\dagger} & \mathbf{S}_{cc}^{\dagger} \end{pmatrix}. \quad (2.5)$$

The matrix β is diagonal and of dimension $N_c \times N_c$; its elements $\beta_i = \pi[-2(E - E_i)]^{-1/2}$ are the Coulomb phase parameters in each closed channel. These quantities vary strongly with energy near their respective thresholds, and account for nearly all the energy dependence of the physical scattering process. This allows the expression to correctly describe resonant spectra even while the energy dependence of the smooth, short-range scattering matrix is entirely neglected.

The physical significance of the eigenvalues of the scattering matrix, as first realized by Fano [45], centers on the recognition that \mathbf{S} will be diagonal in the representation where the short-range Hamiltonian is diagonal. That is, there exist $N = N_c + N_o$ solutions, the *eigenchannel* solutions Φ_{α} , each of which have a common phase shift $\pi\mu_{\alpha}$ in all physical channels. The scattering matrix can be recovered from the eigenchannel defects μ_{α} by means of a transformation,

$$S_{ii'} = \sum_{\alpha} U_{i\alpha} e^{2i\pi\mu_{\alpha}} (\mathbf{U}^T)_{\alpha i'}. \quad (2.6)$$

The matrix \mathbf{U} is known as the frame transformation matrix as a consequence of its role in transforming from the short-range (“body frame”) diagonal representation to the long-range (“lab frame”) electron-plus-core representation. In the inner region, the

outer electron is moving fast enough that a definite value of the internuclear separation R and orbital angular momentum along the axis Λ can be defined; in the outer region, the electron is moving slowly on the time scale of nuclear motion, and the system is more appropriately described by the ionization channel indices. The rotational and vibrational components of the frame transformation matrix can be separated to give

$$U_{i\alpha} = \langle i|\alpha\rangle = \langle v^+|R\rangle^{(N^+)} \langle N^+|\Lambda\rangle^{(lJ)}. \quad (2.7)$$

The first factor is simply the vibrational wavefunction for the v^+ state, and the second factor is a rotational frame transformation matrix element defined in [27]. Note that this expression assumes that a single value of the orbital angular momentum l is present. If additional partial waves contribute significantly in the outer region, then the form of this transformation becomes more complicated.

The eigenchannel quantum defects, since they are labeled by quantities that are meaningful in the Born-Oppenheimer limit, can be extracted from the bound state potential energy curves of H_2 through their definition given in Eq. 2.1. The actual use of these quantum defects in a numerical frame transformation is problematic owing to the continuous variable R , which effectively necessitates an infinite number of channels to be included in the scattering matrix. In practice, however, a reasonable approximation to the exact frame transformation can be accomplished by truncating the sum over alpha after a relatively small number of vibrational states (usually of the order of one or two dozen per ionic rotational quantum number in this work). The approximate frame transformation matrix is formed from the eigenvectors of the quantum defect matrix, defined by

$$\mu_{v^+N^+,v^{+'}N^{+'}}^{(J')} = \sum_{\Lambda} \langle N^+|\Lambda\rangle^{(lJ')} \left[\int dR \langle v^+|R\rangle^{(N^+)} \mu_{\Lambda}(R) \langle R|v^{+'}\rangle^{N^{+'}} \right] \langle \Lambda|N^{+'}\rangle^{(lJ')}, \quad (2.8)$$

The numerical diagonalization of Eq. 2.8 is generally more convenient than direct construction and diagonalization of the scattering matrix itself.

Because of the weak energy dependence of the quantum defect (see Ref. [37]) a single function for each body frame symmetry, $\mu_\Lambda(R)$, suffices to describe all bound state potential energy curves of the π symmetry, and provides a reasonable approximation to most higher n curves of the σ symmetry. We follow Raoult and Jungen [46] in selecting an eigenquantum defect function derived from fitting to the bound states of the n=6 curve for the σ case, and n=5 for π . Since the $3p\sigma$ state deviates substantially from this simple approximation, and the $2p\sigma$ state also differs qualitatively, peaks associated with resonances in these low-n channels are not expected to be located precisely by this method. Gao and Greene [39] have shown how the frame transformation may be reformulated to account for such energy dependent effects.

The total photoionization cross section is directly proportional to the differential oscillator strength, and is given by the expression

$$\sigma(\omega) = \frac{4\pi^2\omega\alpha}{3(2J_0 + 1)} \sum_J \sum_j |D_j^{(-)phys}|^2 \quad (2.9)$$

where J_0 is the initial total angular momentum state, J is the final angular momentum state, $D_j^{(-)phys}$ is the reduced dipole matrix element between the j -th physical incoming-wave solution and the molecular ground state, ω is the frequency of the absorbed photon, and α is the fine structure constant. $D_j^{(-)phys}$ can be calculated by a channel elimination transformation analogous to that for the physical scattering matrix above,

$$\mathbf{D}^{(-)phys} = \mathbf{D}_o^- - \mathbf{D}_c^- [\mathbf{S}_{cc}^\dagger - e^{2i\beta}]^{-1} \mathbf{S}_{co}^\dagger, \quad (2.10)$$

using the reduced dipole matrix elements for the long-range solutions $D_j^{(-)}$, which can themselves be found from the body-frame dipole matrix elements by application of the frame transformation coefficients [47, 27]. Note that in a real physical system at finite

temperature, more than one J_0 will typically be present, and a final average must be carried out over the initial statistical distribution.

In traditional MQDT, an analogue of the scattering matrix channel elimination procedure is performed to determine the final solutions used in the dipole matrix elements. As before, this allows the N_o physical D_j^{phys} to be factored into the matrix product of a vector consisting of N weakly energy dependent short-range D_j and an N_o by N matrix containing all of the resonant structure. The cross section may then be convolved over some finite width Γ using (for example) a Lorentzian kernel

$$\sigma_{conv}(\omega_0) = \frac{1}{2\pi} \int d\omega \sigma(\omega) \frac{\Gamma}{(\omega - \omega_0)^2 + (\Gamma/2)^2} \quad (2.11)$$

to produce a spectrum that approximates the finite resolution achieved in any actual experiment.

Robicheaux [48] showed that this analytical form for the convolution can be rewritten in the suggestive form (suppressing the sum over J)

$$\sigma_{conv}(\omega_0) = -\frac{4\pi^2\alpha}{3(2J_0 + 1)} \text{Im} \left[\left(\omega_0 + \frac{i\Gamma}{2} \right) \sum_j \int dE |D_j^{(-)}|^2 \left(E_g + \omega_0 + \frac{i\Gamma}{2} - E \right)^{-1} \right] \quad (2.12)$$

where $E = E_g + \omega$ is the energy of the final state and E_g is the ground state energy. The sum and integration can be formally carried out to yield a new formula which involves the Coulomb functions defined at *complex* electron energies $E = E_r + \frac{i\Gamma}{2}$. Robicheaux's original expression for this preconvolved cross section, after rearrangement and the application of a matrix identity, can be written as

$$\sigma_{conv}(\omega_0) = -\frac{4\pi^2\alpha}{3(2J_0 + 1)} \text{Im} \left[\left(\omega_0 + \frac{i\Gamma}{2} \right) \sum_j D_j^{(-)*} \sum_k \left((S^\dagger - e^{2i\beta})^{(-1)} (S^\dagger + e^{2i\beta}) \right)_{j,k} D_k^{(-)} \right] \quad (2.13)$$

Unlike the partitioning scheme for channel elimination (as in Eq. (2.4), this formula treats open and closed channels on an equal footing. In essence Eq. (2.13) relies on the exponential to naturally close a channel every time its argument β (a complex generalization of the phase parameter) switches from being almost real at energies below the channel threshold to having a large imaginary component at energies above the threshold. Although the exact expression derived by Robicheaux for β is complicated to evaluate, the approximation

$$\beta_j = \pi\kappa_j, \quad E_r - E_j < 0 \quad (2.14)$$

$$\beta_j = i\infty, \quad E_r - E_j > 0 \quad (2.15)$$

can be used in its place. Here $\kappa_j = 1/\sqrt{-2(E - E_j)}$ is a complex generalization of the effective quantum number in channel j , with the branch chosen such that $\text{Re } \beta_j > 0$ when $E_r - E_j < 0$.

2.4 Application: HD photoionization spectrum

The experimental photoionization spectrum of HD was first observed at high resolution by Dehmer and Chupka [49], and theoretically modeled to a high degree of accuracy by Du and Greene [50]. In this section, we revisit the HD problem using Robicheaux's faster, more direct reformulation of MQDT to generate a much broader range of the photoabsorption spectrum. The decision to return to this system is motivated by several factors. First, high resolution experimental data exists for both the photoionization and photoabsorption cross-sections, and it provides a qualitative measure of the influence of competing dissociation channels or other decay pathways. This allows us to study the anticipated failure of the Ref. [50] implementation of energy independent MQDT. Discrepancies are expected in the neighborhood of strong coupling to the dis-

sociative regions of the potential energy surface, where $g-u$ symmetries become mixed, and where the $1s\sigma$ potential curve may no longer adequately suffice to describe the core electronic state. Second, most of the peaks in the experimental spectrum of HD have remained unassigned, or have only tentative spectroscopic labels, and the present study can identify them with minimal ambiguity. Third, this comparatively straightforward application offers a reasonable opportunity to assess the speed and robustness of the preconvolution variant of MQDT, with the intent of considering it for more general application to other molecular problems in the future.

Below the first ionization threshold, located at 124568.5 cm^{-1} , the spectrum is discrete, consisting of isolated bound states. The preconvolution algorithm describes this region equally well, but owing to our primary interest in the photoionization spectrum, discrete photoabsorption will not be discussed further here. At higher energies, the spectrum consists of sets of Rydberg series that converge to thresholds associated with rovibrational states of the residual ion. Because the vibrational levels are more widely spaced than the rotational levels by approximately an order of magnitude ($\sim 2000\text{ cm}^{-1}$ vs. $\sim 200\text{ cm}^{-1}$), ionization thresholds appear as neighboring pairs, with all allowed transitions corresponding to an ionic rotational state of either $J + 1$ or $J - 1$ (since the Rydberg electron is restricted to the p-wave solutions excited when an HD ground state electron absorbs a single VUV photon). To simulate the results of a spectrum taken at 78 K, the contributions from the three energetically accessible initial rotational states, labeled by their total angular momentum as $J_0=0, 1,$ and 2 are weighted by the Boltzmann statistical factors 61.9%, 35.8%, and 2.2%, respectively. This results in four distinct thresholds, each with up to three attached series (R, Q, and P branches), which originate from each vibrational state of the core.

Much of the complexity of the photoionization spectrum arises in regions where peaks in one series are perturbed by the lower- n resonances of a higher threshold that lie at roughly the same energy. In such cases, spectral features can become so strongly

mixed as that any formal spectroscopic assignments would be somewhat arbitrary. A common example occurs when a lower- n resonance appears just slightly below a higher- n threshold, such that its width is less than the energy separations of the near-threshold series. In this instance, the low- n resonance will be distributed over many adjacent peaks in the series, causing the total number of such peaks to be increased by one and uniformly enhancing their intensity, yet no one peak can be unambiguously assigned to the perturber.

To a limited extent, the spectrum exhibits repeated patterns attributable to the nearly uniform separation between the first few vibrational levels. As a result, a subsection of the total spectrum that spans one vibrational energy spacing serves to provide a qualitatively representative measure of accuracy over a broader range. We have chosen to focus on the spectrum in the energy regime near the second ($v^+ = 1$) set of rovibrational thresholds, from 125500 cm^{-1} to 127300 cm^{-1} .

Figures 2.4-2.7 show the theoretical results superimposed on the experimental data points. Since the experiment does not provide an absolute normalization for the intensity, we have normalized this data to match the theoretical cross-section at 127000 cm^{-1} . The peaks in Figure 1 have been labeled through the application of a technique detailed in [37] which involves searching for the roots of a determinantal equation and examining the magnitude of the coefficients in each closed channel. As n becomes large (≥ 10), the coupling (as noted earlier) undergoes a transition from Hund's case b (where the projection of the angular momentum of the Rydberg electron along the internuclear axis Λ is a "good" quantum number) to Hund's case d (where the preferred quantum number is the rotational state of the core). Although this decoupling occurs gradually, we adopt here the convention of describing resonances of $n < 10$ according to the first case, and $n > 10$ in terms of the second.

In Figures 2.4 - 2.7 several peaks are labeled that exhibit some significant discrepancies between theory and with experiment. These discrepancies likely arise from our

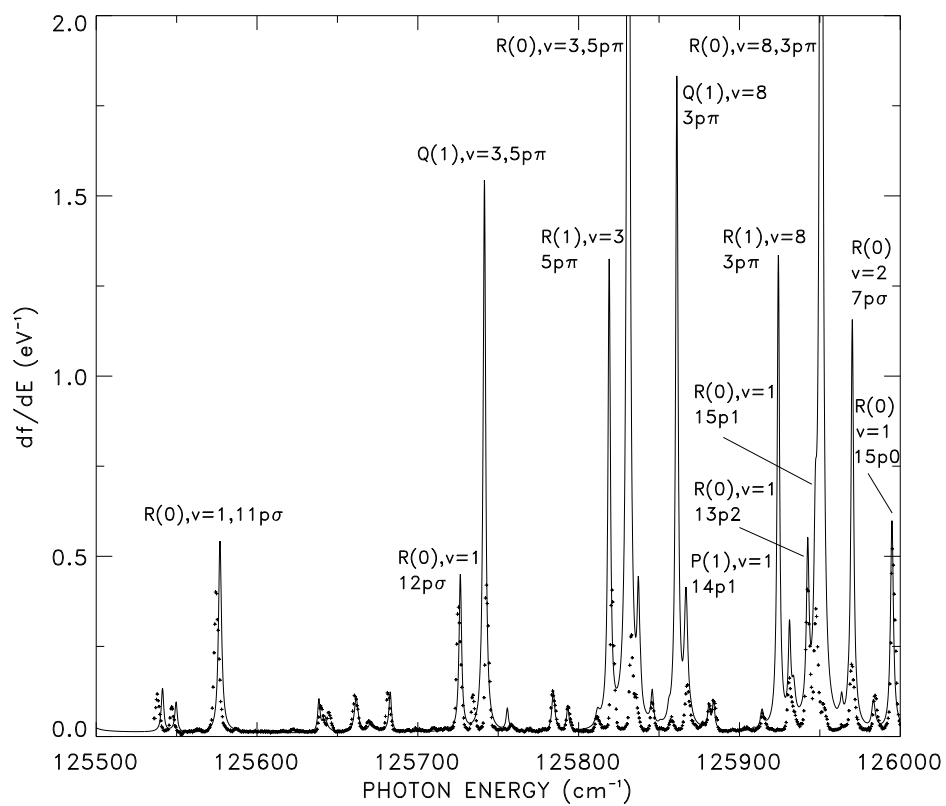


Figure 2.4: Experimental[49] and preconvolved theoretical oscillator strength [51] for HD photoionization between 125500-126000 cm^{-1} photon energy.

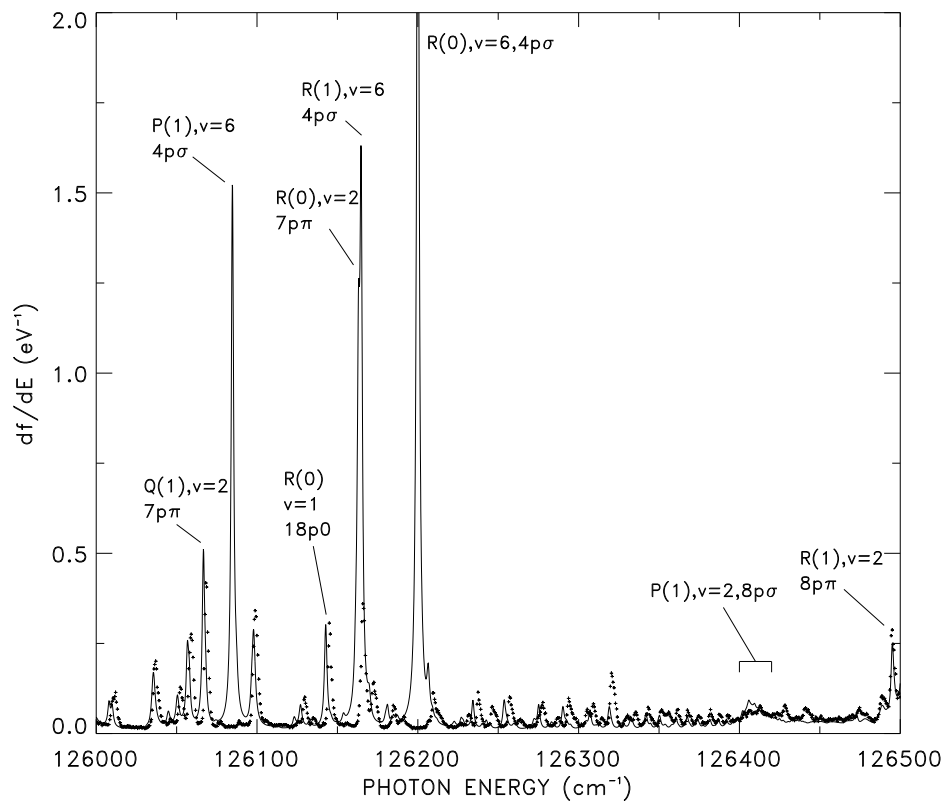


Figure 2.5: Experimental[49] and preconvolved theoretical oscillator strength [51] for HD photoionization between 126000-126500 cm^{-1} photon energy.

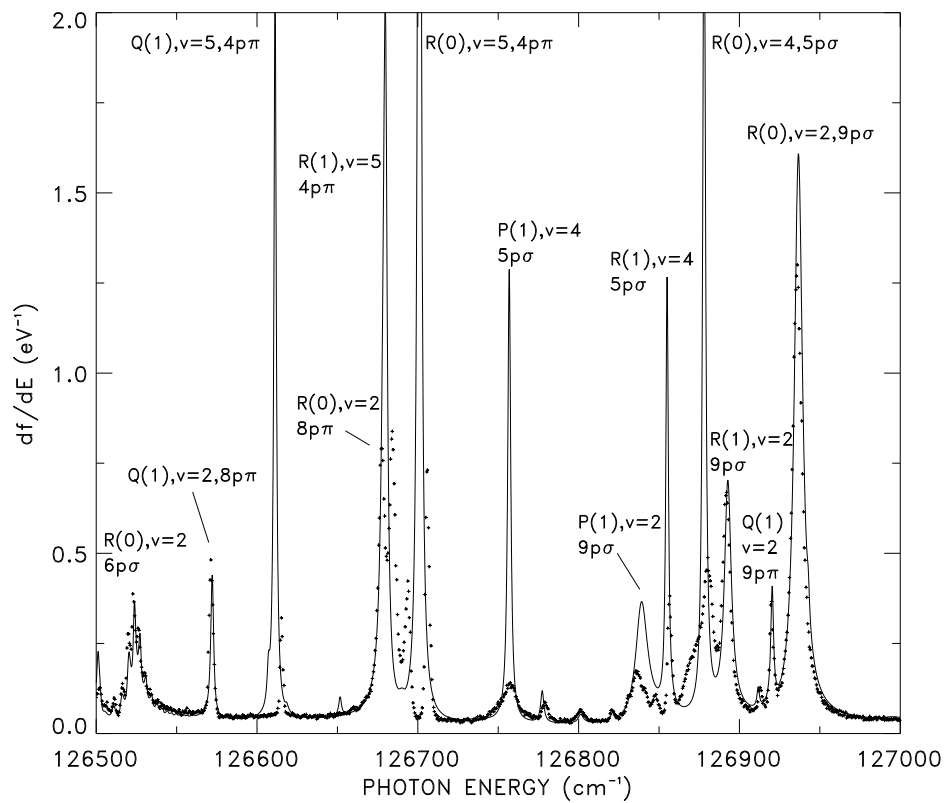


Figure 2.6: Experimental[49] and preconvolved theoretical oscillator strength [51] for HD photoionization between 126500-127000 cm^{-1} photon energy.

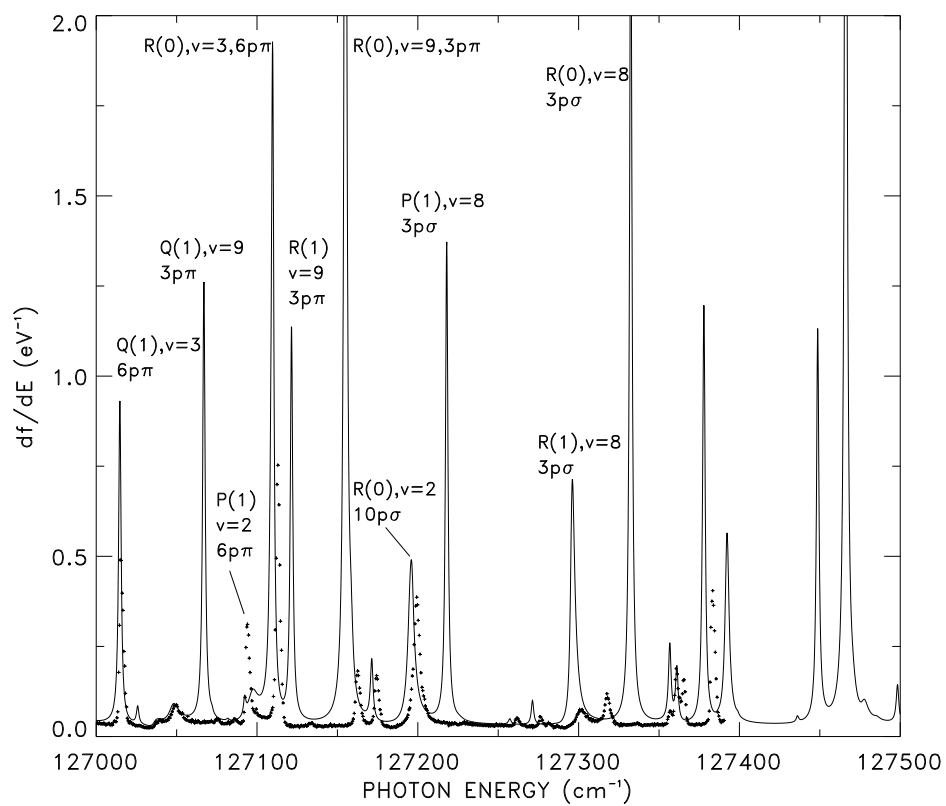


Figure 2.7: Experimental[49] and preconvolved theoretical oscillator strength [51] for HD photoionization between 126000-127500 cm^{-1} photon energy.

neglect of competing predissociation processes in the MQDT calculations. As previously shown by Du and Greene[50], departures from linear absorption in the experiments from photon energies ~ 12600 to greater than 12700 cm^{-1} are also a potential problem. Regarding predissociation, for example, the resonances labeled R(0), R(1), and Q(1) that are assigned to perturbers associated with $v = 3 - 8$ ionic cores are likely to be affected by coupling with either the repulsive, dissociative inner wall of the potential energy surface via the Coriolis interaction (for $\Lambda \neq \Lambda'$), or the outer potential regions where $n\lambda n'\lambda'$ doubly-excited potential curves are known to intersect and strongly perturb the Rydberg potential surface. Such examples of channel interactions are well-documented in H_2 (e.g. the $3p\sigma$ - $3p\pi$ Coriolis-type predissociation discussed in [52], and predissociation of the $3p\pi$, $v = 8$ and $4p\pi$, $v = 5$ states discussed in [53] and [54]). Although these two mechanisms appear to be distinct, MQDT in principle allows a unified description of *joint* Coriolis interactions and electronic core excitations.

Comparison of our results with experiment in Figure 2.4 shows that many of the observed resonances are in good agreement in terms of position and intensity. Most of these resonances are assigned to those classified in the Hund's case d limit and they also have low vibrational excitation. Discrepancies in intensities, however are apparent for the strong $v=3$ resonances predicted at 125750 and 125830 cm^{-1} , as well as the $v=8$ set between 125860 and 125900 cm^{-1} . These resonances are associated with $5p\pi$, $v = 3$ interlopers. For HD it is somewhat surprising (but not unprecedented) that Rydberg states attached to ionic cores with vibrational quanta as low as $v = 3$ excitation will strongly sample the dissociative regions of the potential energy surfaces, resulting in a significant competition with the autoionization channel. The increase in the effective, non-adiabatic couplings in HD may therefore be related to the breakdown of the g-u inversion symmetry, particularly near its dissociative limits; for the corresponding peaks in the H_2 spectrum the predissociation is only moderate [55].

Another class of discrepancy in Figure 2.4 is typified by the predicted R(0), $v = 2$,

$7p\sigma$ interloper at 125970 cm^{-1} , which, while in good agreement in terms of position, is too intense. This may be due to the breakdown of symmetry, or else to the non-linearity of the intensity dependence on the cross section arising from saturation effects [50]. (The results of Glass-Maujean [55] imply that ionization prevails for the $7p\sigma$ series in H_2 except in cases where the peaks are strongly mixed with another series.)

Figures 2.5 - 2.7 show a comparison of the present theory with the remaining range of experiment considered here, leading up to 127500 cm^{-1} . Figure 2.5 shows an increasing number of low- n , high- v interlopers predicted by theory with minimal correlation to resonance observed in the experiment. It is also apparent that shifting of many predicted resonances $\sim 3\text{-}5\text{ cm}^{-1}$ compared to experiment occurs near the $v = 1$ threshold at 126600 cm^{-1} (shifts of this magnitude are also noticeable for some of the resonances in Figure 2.4 as well). The origin of these shifts is not certain, although Ref. [50] pointed out that they are likely due to our neglect of energy dependence in the quantum defects, or else associated with random slippage errors in the experimental wavelength calibration.

The discrepancies seen in Figure 2.6 are most apparent for the very strong resonances predicted at 126610 , 126680 , and 126700 cm^{-1} , respectively. These resonances are associated with $4p\pi$, $v = 5$ interlopers which can predissociate. This resonance and intensity pattern parallels the three predicted $5p\pi$, $v = 3$ interlopers shown in Figure 2.4, perhaps strengthening the conclusion that those are strongly predissociated as well.

In Figure 2.7 one observes a complete breakdown of agreement between the theoretical predictions and experiment beyond $\sim 127200\text{ cm}^{-1}$. This must be attributed to my neglect of predissociation processes, particularly since the predicted resonances are associated with interlopers which have very high vibrational excitation, for example, states with $3p\lambda$, $v = 8 - 9$. These states would predissociate primarily through Coriolis coupling with $n\sigma$ states of comparable total energy.

In summary, disagreement between the MQDT calculations and experiment is probably partly attributable to the neglect of predissociation via the Coriolis interaction and channel-coupling with two-electron excited core states. In limited spectral regions, departures from linearity in the original experimental conditions could also be a source of discrepancy. In chapter 5, approaches to the treatment of predissociation will be reconsidered in greater detail.

Within regions of the spectrum dominated by high- n resonances, however, the frame transformation-based MQDT method remains impressively accurate. The very recent work of Merkt and coworkers [56] provides a persuasive example of the capabilities of the frame transformation to describe even densely spaced resonances in the near-threshold regime. Figure 2.8 shows the experimental photoionization spectrum plotted in a narrow region near the $v = 1$, $np0$ threshold, where the Rydberg series has many sharp and narrow resonances. Just above the threshold is a complex resonance arising from the perturbation of the $v = 1$, $np2$ series (converging to a threshold at 789.847 Å) by an interloper attached to the $v = 2$ threshold. Each of the modulated groupings of peaks below the threshold at 790.630 Å can similarly be understood as a complex resonance arising from the mixing of the overlapping $v = 1$, $np0$ and $v = 1$, $np2$ series. The theory (b) in 2.8 is a reproduction of the result in [50], calculated at too coarse a mesh to identify any of these high- n structures. Figure 2.9 shows the same spectrum recalculated on a much finer mesh; the positions as well as the intensity modulation and shifting line profiles across the complex resonance sets are all well-described by the theory, aside from a few very weak and broad features in the experimental spectrum. (The disagreement in intensity for the Q(1), $v = 2$ $8p\pi$ peak at 790.07 Å is presumably due to predissociation.)

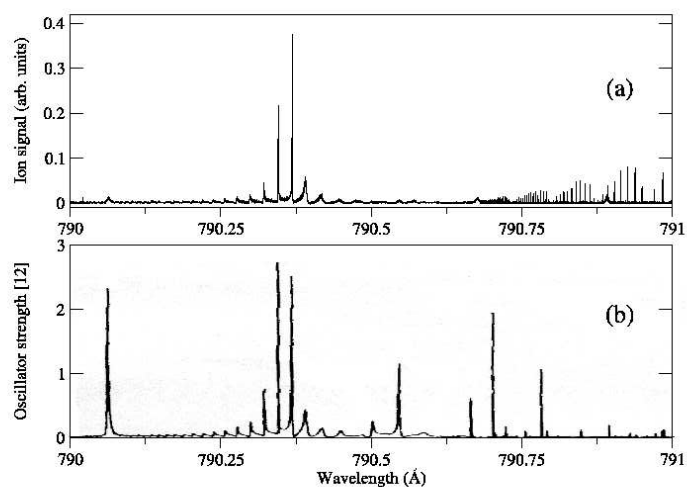


Figure 2

Figure 2.8: Ultra high resolution experimental (a) [56] and theoretical (b) oscillator strength for HD photoionization near the $v=1$ threshold, using theory from the mid-1980s by Du and Greene [50].

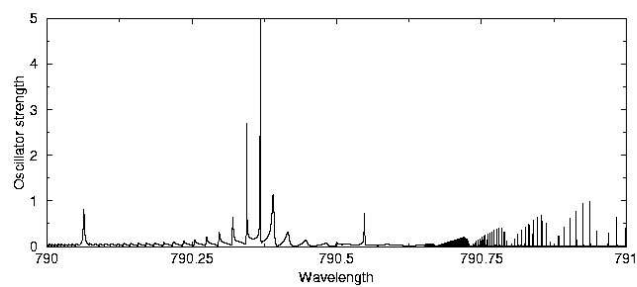


Figure 2.9: Recent recalculation of the theoretical oscillator strength by the same method, on a much finer grid and at a rotational temperature (25 K) appropriate for the newer experiment.